Available online at www.sciencedirect.com
SCIENCE DIRECT®
ELSEVIER
Journal of Contaminant Hydrology 67 (2003) 133–157
JOURNAL OF Contaminant Hydrology
www.elsevier.com/locate/jconhyd

Entrapment and dissolution of DNAPLs in heterogeneous porous media

Scott A. Bradford[a,*], Klaus M. Rathfelder[b], John Lang[b], Linda M. Abriola[b]

[a] *George E. Brown, Jr., U.S. Salinity Laboratory, USDA, ARS, 450 W. Big Springs Road, Riverside, CA 92507-4617, USA*
[b] *Department of Civil and Environmental Engineering, University of Michigan, 181 EWRE, 1351 Beal Avenue, Ann Arbor, MI 48109-2125, USA*

Received 9 October 2001; accepted 28 March 2003

Abstract

Two-dimensional multiphase flow and transport simulators were refined and used to numerically investigate the entrapment and dissolution behavior of tetrachloroethylene (PCE) in heterogeneous porous media containing spatial variations in wettability. Measured hydraulic properties, residual saturations, and dissolution parameters were employed in these simulations. Entrapment was quantified using experimentally verified hydraulic property and residual saturation models that account for hysteresis and wettability variations. The nonequilibrium dissolution of PCE was modeled using independent estimates of the film mass transfer coefficient and interfacial area for entrapped and continuous (PCE pools or films) saturations. Flow simulations demonstrate that the spatial distribution of PCE is highly dependent on subsurface wettability characteristics that create differences in PCE retention mechanisms and the presence of subsurface capillary barriers. For a given soil texture, the maximum and minimum PCE infiltration depth was obtained when the sand had intermediate (an organic-wet mass fraction of 25%) and strong (water- or organic-wet) wettability conditions, respectively. In heterogeneous systems, subsurface wettability variations were also found to enhance or diminish the performance of soil texture-induced capillary barriers. The dissolution behavior of PCE was found to depend on the soil wettability and the spatial PCE distribution. Shorter dissolution times tended to occur when PCE was distributed over large regions due to an increased access of flowing water to the PCE. In heterogeneous systems, capillary barriers that produced high PCE saturations tended to exhibit longer dissolution times.
Published by Elsevier B.V.

Keywords: Nonaqueous phase liquid (NAPL); Dissolution; Entrapment; Wettability; Heterogeneity; Interfacial area

* Corresponding author. Tel.: +1-909-369-4857; fax: +1-909-342-4963.
E-mail address: sbradford@ussl.ars.usda.gov (S.A. Bradford).

0169-7722/$ - see front matter. Published by Elsevier B.V.
doi:10.1016/S0169-7722(03)00071-8

1. Introduction

The improper storage and disposal of nonaqueous phase liquids (NAPLs) has resulted in widespread contamination of the subsurface environment (National Research Council, 1994). NAPLs migrate downward through the heterogeneous subsurface under the influence of gravity and capillary forces. Upon reaching the saturated zone, an NAPL may move laterally within the capillary fringe zone at the water table or, for denser than water NAPLs (DNAPLs), the saturated zone may not act as an impediment to vertical migration and the DNAPL may continue to move downward. As the NAPL migrates, capillary forces act to retain a residual portion of the mass as ganglia in the center of the pore space (Chatzis et al., 1983) or as films coating NAPL-wet solids. In soil column experiments, entrapped residual NAPL saturations typically range from 5% to 35% of the pore space (Wilson et al., 1990; Powers et al., 1992, 1994a,b; Bradford et al., 1999). When an infiltrating NAPL encounters an interface of capillary contrast, the NAPL tends to accumulate in pools and spread laterally along such interfaces (Wilson et al., 1990; Bradford et al., 1998). If such an interface is tilted, the infiltrating fluid will be diverted and flow down the interface as capillary diversion. Capillary barriers occur naturally in heterogeneous systems due to differences in soil texture (e.g., Kueper et al., 1989, 1993; Wilson et al., 1990; Kueper and Frind, 1991; Poulsen and Kueper, 1992; Essaid et al., 1993; Dekker and Abriola, 2000) and/or porous medium wettability characteristics (Bradford et al., 1998). Downward migration of NAPL will continue in the subsurface until the NAPL is completely retained as entrapped residual or pooled NAPL. This final distribution of NAPL is referred to as the NAPL source zone.

The slow partitioning of NAPL in the source zone to flowing water serves as a persistent source of groundwater contamination. Regulated exposure levels for many NAPLs are several orders of magnitude below their solubility limits. Subsurface NAPL contamination is therefore a problem of serious concern at hazardous waste sites. Experimental studies have been undertaken to investigate the dissolution behavior of uniformly distributed residual NAPL in soil columns (e.g., Hunt et al., 1988; Miller et al., 1990; Parker et al., 1991; Guarnaccia et al., 1992; Powers et al., 1991, 1992, 1994a,b; Imhoff et al., 1994, 1997; Rixey, 1996). Most of these studies have been conducted using water-wet glass beads or silica sands. Results from these studies indicate that dissolution behavior depends on system hydrodynamics, NAPL saturation and composition, and soil grain-size distribution characteristics. However, these studies have not produced clear consensus on the effect of soil grain-size distribution parameters and NAPL saturation on dissolution behavior (cf., Miller et al., 1998; Bradford et al., 2000).

Laboratory-scale dissolution experiments have also been conducted in larger-scale systems (Anderson et al., 1992; Geller and Hunt, 1993; Powers et al., 1998; Saba and Illangasekare, 2000). Both Geller and Hunt (1993) and Anderson et al. (1992) employed homogeneous media with cylindrical regions of residual NAPL blobs embedded in the center. Geller and Hunt (1993) attributed reductions in the dissolution mass transfer rate to the reduced effective permeability within the region of residual NAPL. In contrast, Anderson et al. (1992) concluded that reductions in dissolution mass transfer rate in their experiments were attributed to dispersion and dilution of contaminated water. Saba and Illangasekare (2000) reported on two-dimensional dissolution experiments in which the

residual NAPL was entrapped in rectangular shaped source zones of various lengths. They found that the experimental lumped mass transfer coefficient increased with increasing size of the contaminant source zone. Powers et al. (1998) conducted dissolution experiments in heterogeneous systems consisting of NAPL entrapped at high saturation in coarse-textured lenses. They found that initial dissolution rates could be adequately predicted by accounting for system hydrodynamics (variations in intrinsic and effective permeabilities). At low NAPL saturations, however, rate-limited NAPL dissolution was found to become important.

Numerical models have been used to predict the entrapment and dissolution behavior of NAPLs in heterogeneous porous media (Mayer and Miller, 1996; Berglund, 1997; Dekker and Abriola, 2000). These studies indicate that increasing the variance of the hydraulic conductivity distribution (physical heterogeneity) tends to increase the dissolution time. Correlations for the lumped mass transfer coefficient incorporated into these models were developed from small-scale soil column experiments with uniform residual NAPL saturations. Application of these relationships to heterogeneous systems often requires extrapolation to much higher NAPL saturations and porous media characteristics beyond the scope of experimental conditions considered in correlation development. Not surprisingly, Mayer and Miller (1996) reported that differences in the predicted dissolution behavior for various mass transfer coefficient correlations increased with increasing degree of physical heterogeneity.

In natural subsurface systems, highly irregular NAPL distributions have been observed (Poulsen and Kueper, 1992; Essaid et al., 1993). Variations in soil texture and wettability may account for some of these irregularities. In comparison to information on soil texture, there is a paucity of data on subsurface wetting properties and no systematic studies of NAPL-water contact angle variations have been reported. Heterogeneity of subsurface wettability characteristics may occur at hazardous waste sites as a result of variations in aqueous chemistry (Demond et al., 1994), mineralogy (Anderson, 1986), organic matter distributions (Dekker and Ritsema, 1994), and contaminant aging (Powers and Tamblin, 1995). Bradford et al. (1999) presented soil column entrapment and dissolution data for tetrachloroethylene (PCE) in soils representative of a range of grain-size and fractional wettability characteristics. Organic entrapment and dissolution rates were found to depend strongly on wettability and grain-size distribution characteristics. These observations suggest that the superposition of soil texture and wettability properties in heterogeneous environments will likely determine the entrapment and dissolution behavior of NAPLs. To date, relatively little research has explored the influence of subsurface wettability variations on NAPL distribution and remediation.

The objective of this work is to explore the entrapment and dissolution behavior of DNAPLs in porous media containing spatial variations in soil texture and wettability. Conceptual models for NAPL entrapment and dissolution that were developed from experimental data (Bradford and Abriola, 2001) were implemented into existing two-dimensional NAPL flow (Abriola et al., 1992) and transport (Abriola et al., 1997; Rathfelder et al., 2000) simulators. The entrapment model presented by Bradford et al. (1998) was extended to account for the nonlinear influence of wettability on NAPL entrapment. The dissolution model presented by Bradford and Abriola (2001), which utilizes independent estimates of the film mass transfer coefficient and interfacial area, was

modified to account for both entrapped and continuous (immobile films and NAPL pools) NAPL saturations. Independently determined hydraulic properties, residual saturations, and dissolution parameters for soils encompassing a range of grain-size and wettability characteristics are used herein, in conjunction with the refined numerical simulators. Emphasis is placed upon NAPL recovery; sorption/desorption processes are not considered in the simulations.

2. Models of NAPL entrapment and dissolution

2.1. Entrapment

MVALOR, a two-dimensional three-phase immiscible flow simulator, is employed herein to investigate the entrapment behavior of PCE in saturated systems. A description of the numerical methods, model verification and testing, and example model applications for this simulator are available in the literature (Abriola et al., 1992; Abriola and Rathfelder, 1993; Demond et al., 1996; Rathfelder and Abriola, 1998; Bradford et al., 1998; Dekker and Abriola, 2000). In this work, the model will be used to solve the coupled mass conservation equations for the NAPL and aqueous phases (e.g., Abriola, 1989):

$$\frac{\partial}{\partial t}(\varepsilon \rho_i S_i) = \nabla \left[k \frac{\rho_i k_{ri}}{\mu_i} (\nabla P_i - \rho_i g \nabla z) \right] + \rho_i R_i \tag{1}$$

where S is the saturation, P (M L^{-1} T^{-2}) is the pressure, ε is the porosity of the medium, μ (M L^{-1} T^{-1}) is the viscosity, k (L^2) is the intrinsic permeability, ρ (M L^{-3}) is the density, g (L T^{-2}) is the acceleration due to gravity, R (T^{-1}) is the source/sink term, z (L) is the positive downward vertical direction, ∇ is the gradient operator ($\partial/\partial x$, $\partial/\partial z$; x is the horizontal direction), and the subscript i denotes the distinct fluid phases (i.e., i = o,w for organic and water, respectively). These mass conservation equations require that $S_o + S_w = 1$.

To account for the influence of wettability on NAPL migration, hysteretic fractional wettability hydraulic property models (Bradford and Leij, 1996; Bradford et al., 1997) that were developed from careful comparison to experimental data were incorporated into MVALOR (Bradford et al., 1998). Measured capillary pressure (P_{ow})–saturation data were described with the modified van Genuchten model (Bradford and Leij, 1995a) (cf. Table 1). Relative permeability relations were estimated from capillary pressure data according to the pore-size distribution model presented by Bradford et al. (1997). This model accounts of the influence of wettability on the relative permeability relations. The model predicts that for a given saturation and saturation history, an increasing organic-wet fraction tends to decrease the NAPL relative permeability and increase the water relative permeability.

In fractional wettability porous media, the residual water (S_{rw}) and NAPL (S_{ro}) saturations consist of the sum of immobile and entrapped saturations. Values of S_{rw} and S_{ro} that are utilized herein were obtained from measured capillary pressure–saturation

Table 1
Hydraulic properties of experimental systems

F_o	ε	n	α_d (cm^{-1})	α_i (cm^{-1})	λ_d (cm)	λ_i (cm)	S_{rw}	S_{ro}	k (m^2)
F20-F30									
0.00	0.315	5.875	0.124	0.264	0.000	0.000	0.159	0.100	4.08e – 10
1.00	0.328	5.875	0.124	0.264	9.570	10.00	0.100	0.065	4.08e – 10
F35-F50									
0.00	0.313	5.359	0.055	0.129	0.000	0.000	0.040	0.200	6.37e – 11
0.25	0.313	5.359	0.055	0.129	6.740	6.090	0.014	0.109	6.37e – 11
0.50	0.313	5.359	0.055	0.129	14.30	12.50	0.045	0.100	6.37e – 11
0.75	0.315	5.359	0.055	0.129	18.87	17.23	0.084	0.066	6.37e – 11
1.00	0.321	5.395	0.055	0.129	20.44	22.58	0.050	0.050	6.37e – 11
F70-F110									
0.00	0.331	9.264	0.022	0.044	0.000	0.000	0.245	0.245	4.68e – 12
0.25	0.325	9.264	0.022	0.044	20.06	17.64	0.080	0.080	4.68e – 12
0.50	0.330	9.264	0.022	0.044	37.32	40.30	0.080	0.110	4.68e – 12
1.00	0.342	9.264	0.022	0.044	59.67	66.51	0.180	0.070	4.68e – 12

data. An immobile wetting fluid residual occurs due to the presence of thin films (water or NAPL) coating solid surfaces, whereas entrapped nonwetting fluid residual occurs in larger portions of the pore space as a result of capillary instabilities as wetting fluid invades (Chatzis et al., 1983). Bradford et al. (1998) postulated that entrapped (S_{ot}) and immobile (S_{oi}) residual NAPL saturations can be linearly related to the NAPL-wet sand mass fraction (F_o) as $(1-F_o)S_{ro}$ and F_oS_{ro}, respectively. Recent analysis of measured residual NAPL saturation values and dissolution behavior in fractional wettability media, however, suggests that the magnitude of S_{ot} and S_{oi} vary in a more complex and nonlinear manner with F_o and soil grain-size distribution (Bradford et al., 1999). It is assumed herein that entrapped and immobile residual NAPL saturations are given as $\omega_o S_{ro}$ and $(1-\omega_o)S_{ro}$, respectively. Here, ω_o is used to account for the nonlinear influence of fractional wettability on entrapped and immobile residual saturations. Based upon the fitted values of ω_o to fractional wettability dissolution data (developed from 20 soil column experiments using various-sized Ottawa sands, including those listed in Table 1), the following empirical correlations were developed by Bradford and Abriola (2001):

$$\omega_o = (1-F_o)^{11.44} \quad d_{50} < 0.071$$

$$\omega_o = (1-F_o)^{42.79} \quad d_{50} \geq 0.071 \tag{2}$$

Values of the entrapped (S_{wt}) and immobile (S_{wi}) water saturation were determined analogously to S_{ot} and S_{oi} by reversing the roles of NAPL and water. When $S_{ot} = \omega_o S_{ro}$, it is assumed that all the accessible pore space has contacted NAPL. To account for hysteretic effects on S_{ot}, the procedures of Land (1968) and Parker and Lenhard (1987) are employed. Hysteretic effects on S_{oi} are modeled by multiplying $(1-\omega_o)S_{ro}$ by $S_{omax}/(1-S_{wi})$; here S_{omax} is the historic maximum NAPL saturation. This approach assumes that S_{oi} is proportional to the drainage pore space that is accessible to the NAPL.

A qualitative experimental validation of MVALOR was recently provided by O'Carroll et al. (2001). These authors presented a comparison between measured and MVALOR-simulated PCE infiltration and redistribution in a two-dimensional heterogeneous system containing spatial variations in soil texture (Ottawa sands given in Table 1) and wettability. The MVALOR model results compared quite well with the experimental data when using independently determined hydraulic properties.

2.2. Dissolution

The MISER model is employed herein to investigate the dissolution behavior of PCE in saturated systems. A description of the numerical methods, model verification and testing, and example model applications for this simulator are available in the literature (Abriola et al., 1997; Rathfelder et al., 2000, 2001). MISER currently solves a coupled system of two-phase flow (air–water) and multicomponent transport/reaction equations, subject to rate-limited mass transfer. The model also incorporates an immobile NAPL phase. In MISER, a transport equation for a given component in the aqueous phase is modeled as

$$\frac{\partial}{\partial t}(\varepsilon S_w C) = \nabla(\varepsilon S_w D_h \cdot \nabla C) - \nabla(q_w C) + \sum_{\gamma} E_{\gamma w} + B \tag{3}$$

where q_w (L T^{-1}) is the Darcy velocity vector, D_h (L^2 T^{-1}) is the component hydrodynamic dispersion coefficient tensor, C (M L^{-3}) is the component concentration, B (M T^{-1} L^{-3}) is the net rate of biological transformation of the component, and $E_{\gamma w}$ (M T^{-1} L^{-3}) is the interphase mass transfer rate of the component across the aqueous and γ phase interface. A similar equation is written for the component mass balance equation for the NAPL phase. In this case, however, the advective and dispersive solute fluxes are set equal to zero.

Nonequilibrium dissolution is accounted for in MISER using an quasi-steady state approximation of Fick's first law of diffusion. The dissolution model presented below is an adaptation of the model presented by Bradford and Abriola (2001) that was developed to describe the soil column dissolution behavior of residual NAPL entrapped in fractional wettability porous media. This model is modified below to explore the dissolution behavior of NAPLs in heterogeneous systems. In such systems, the final NAPL saturation distribution from MVALOR serves as the initial condition for the MISER simulations. The NAPL saturation (S_o) at a particular location is assumed to be the sum of contributions from NAPL entrapped as ganglia in water-wet pores (S_{ot}) and as continuous NAPL phase (S_{oc}) occurring as immobile films coating NAPL-wet solid surfaces or free product NAPL pools. The determination of S_{ot} was discussed above in Section 2.1. The value of S_{oc} is determined as $S_o - S_{ot}$.

The following expression is employed herein to describe the mass exchanged per unit time per unit volume between the NAPL and aqueous phases (E_{ow}) (Bradford and Abriola, 2001):

$$E_{ow} = \frac{-\partial(\varepsilon S_o \rho_o)}{\partial t} = k_{ow}(\alpha A_{ow}^t + \beta A_{ow}^c)(C_e - C) \tag{4}$$

Here k_{ow} (L T^{-1}) is known as the film mass transfer coefficient, A^t_{ow} (L^{-1}) is the NAPL-water interfacial area per unit volume of porous media attributed to entrapped ganglia, A^c_{ow} (L^{-1}) is the NAPL-water interfacial area per unit volume of porous media attributed to the continuous NAPL phase, C_e (M L^{-3}) is the equilibrium solubility concentration that approximates the concentration at the NAPL-water interface, and α and β are parameters to account for the fact that only a fraction of the interfacial area is exposed to mobile water.

Independent estimates for k_{ow} and the NAPL-water interfacial area are utilized herein. The value of k_{ow} is estimated using a slightly modified form of the dimensionless correlation developed by Powers et al. (1994b). Powers et al. (1994b) measured the dissolution behavior of solid naphthalene spheres, with a known size and interfacial area that had been embedded in sandy porous media. Measured values of k_{ow} from this study were assumed to be independent of NAPL configuration because the interfacial area was well characterized. These authors established a dimensionless power function correlation that relates k_{ow} measurements to experimental porous medium (median grain size) and hydrodynamic (aqueous phase pore water velocity) characteristics. Bradford and Abriola (2001) modified this expression to account for the reported dependence of k_{ow} on NAPL diffusivity and viscosity (Imhoff et al., 1997).

The influence of NAPL configuration on dissolution behavior is explicitly modeled herein by accounting for temporal changes in the NAPL-water interfacial area. The determination of interfacial area attributed to the entrapped ganglia (A^t_{ow}) was recently discussed in detail by Bradford and Abriola (2001). At a particular location, entrapped NAPL is initially distributed among a number of ganglia classes. Each ganglia class consists of spherical singlets associated with a different saturation-dependent radius and NAPL saturation (Powers et al., 1991, 1994a,b). The initial values of saturation-dependent singlet class radii are estimated from NAPL-water capillary pressure (P_{ow})–water saturation (S_w) data using Laplace equation for capillarity and assuming that the ganglia are entrapped in the largest portions of the pore space (i.e., in the saturation range $1 - S_{ot} < S_w < 1$) (Bradford and Leij, 1997). The initial interfacial area per unit volume for each pore class is then estimated as the product of the surface area of the sphere and the number of spheres per unit volume. Bradford and Abriola (2001) reported favorable agreement between A^t_{ow} estimates and measurements (entrapped styrene ganglia that had been polymerized in situ, removed from the soil, and then sieved into various ganglia size classes). Both Powers et al. (1994b) and Bradford and Abriola (2001) have used a distribution of NAPL spheres to successfully model the long-term dissolution behavior of entrapped NAPL ganglia.

The value of interfacial area attributed to the continuous NAPL phase, A^c_{ow}, at a given water saturation was estimated from P_{ow}–S_w data. Thermodynamic considerations suggest that the area under a capillary pressure curve is related to the NAPL-water interfacial area (Leverett, 1941; Morrow, 1970; Bradford and Leij, 1997). In this work, an estimate of A^c_{ow} for a particular porous medium is obtained from main imbibition P_{ow}–S_w data as

$$A^c_{ow} = -\frac{\epsilon}{\sigma_{ow}} \int_{\chi}^{S_w} P_{ow}(S)\mathrm{d}S \tag{5}$$

Here the limit of integration χ is assumed to be the value of S_w, where $P_{ow}=0$, σ_{ow} (MT^{-2}) is the interfacial tension, and S is a dummy saturation variable of integration. In water-wet systems, the value of P_{ow} is exclusively positive and χ equals $1-S_{ot}$. In contrast, in fractional wettability systems, the value of P_{ow} can be positive or negative depending on the water saturation and χ tends to decrease with increasing organic-wet solid fraction. Bradford and Abriola (2001) estimated the NAPL-water interfacial area of residual NAPL films coating NAPL-wet solid surfaces in a slightly different manner as the product of the area of drained pore space and the organic-wet mass fraction; Eq. (5) is believed to provide a better description of temporal changes in A_{ow}^{c}.

The above relations provide initial estimates of the interfacial area for a given NAPL saturation. Temporal changes in interfacial area as a result of dissolution are modeled according to the approach presented by Bradford and Abriola (2001). As dissolution proceeds, changes in NAPL saturation during a given time interval (ΔS_o) are evaluated as the sum of changes in the entrapped (ΔS_{ot}) and continuous (ΔS_{oc}) NAPL saturations. Eq. (4) indicates that the values of ΔS_{ot} and ΔS_{oc} will be related to the magnitudes of $(\alpha A_{ow}^{t}\Delta S_o)/(\alpha A_{ow}^{t}+\beta A_{ow}^{c})$ and $(\beta A_{ow}^{c}\Delta S_o)/(\alpha A_{ow}^{t}+\beta A_{ow}^{c})$, respectively. Temporal changes in A_{ow}^{c} for a particular location are calculated with Eq. (5). Hence, A_{ow}^{c} is a function of S_w until S_{oc} is zero, at which time A_{ow}^{c} is set equal to zero. The value of $A_{ow}^{t}$is also modeled as an explicit function of saturation. In this case, the ganglia radii slowly decrease in size as S_{ot} decreases. The saturation dependence of a particular ganglia class radius is related to the initial ganglia class radius and NAPL saturation (Bradford and Abriola, 2001). The interfacial area is then calculated as the product of the surface area of the sphere and the number of spheres per unit volume. Note that only initial ganglia class radii are estimated using capillary pressure data.

Values of α and β are predicted herein from correlations established by Bradford and Abriola (2001) between fitted values and experimental parameters (developed from 20 soil column experiments using various-sized Ottawa sands, including those listed in Table 1). The value of α was found to be inversely related to the normalized mean grain size, suggesting that less mobile water contacts the NAPL ganglia in finer textured soils. The value of β was found to be inversely related to the soil uniformity coefficient and A_{ow}^{c}. These observations suggest that some of the continuous NAPL films are less accessible to a flowing aqueous phase in more graded soils and that the dissolution rate depends nonlinearly on interfacial area.

3. Numerical simulations

3.1. Entrapment

This section discusses the numerical investigation of entrapment behavior of PCE in various subsurface systems. In this work, measured intrinsic permeability, capillary pressure–saturation relations, and residual saturation values for various fractional wettability soils are used as input to MVALOR. These experimental properties were determined independently in soil column experiments. Fractional wettability soils were created by combining various mass fractions of untreated and octadecyltrichlorosilane

(OTS)-treated Ottawa sands. These soils will be designated herein by their sieve sizes (F20-F30, F35-F50, F70-F110, and F35-F50-F70-F110) and their NAPL-wet mass fraction, F_o, or OTS percentage. The intrinsic permeability was measured using the constant flux technique (e.g., Klute and Dirksen, 1986). The capillary pressure–saturation relations and residual saturation were determined on similar soil columns using an automated setup based upon the experimental design presented by Bradford and Leij (1995b) using the pressure cell approach (e.g., Demond and Roberts, 1991). Measured capillary pressure (P_{ow})–saturation data were described with the modified van Genuchten model (Bradford and Leij, 1995a). Table 1 summarizes measured soil intrinsic permeabilities, capillary pressure–saturation curve parameters, and residual saturations that are used below in numerical simulations. Here the capillary pressure parameter n is related to the slope at the inflection point of the P_{ow}–S_w curve (m was chosen to be equal to $1-1/n$), α_d and α_i are drainage and imbibition reciprocal entry pressures, and λ_d and λ_i are the drainage and imbibition shifting parameters. The relevant physical properties of PCE that were employed in simulations are density (1625.0 kg m^{-3}), viscosity (0.00089 kg ms^{-1}), and interfacial tension (0.045 N m^{-1}).

For the simulations discussed below, PCE was introduced at the top (center node in 1D simulations, and center 0.5 m in 2D simulations) of an initially water-saturated model domain for a period of 1.5 days at a constant infiltration rate of 15 l day^{-1} (infiltration velocity of 1.5 and 3.0 cm day^{-1} in 1D and 2D simulations, respectively). Following the PCE release, redistribution occurred for a total simulation time of 360 days. For one-dimensional simulations, the model domain extended 15 m in the vertical direction with a uniform nodal spacing of 0.025 m. A no flow boundary condition for water and PCE was enforced at the top of the model domain (PCE was added using a time-dependent source term), while a constant pressure condition (hydrostatic as referenced to atmospheric pressure at the domain surface) was employed at the bottom boundary. For two-dimensional simulations, a 5-m (vertical) by 3.5-m (horizontal) cross-section model domain was employed. Nodal spacing in the horizontal direction was 0.1 m. To accurately capture capillary barrier behavior in the vicinity of various soil lens, the vertical spacing was set equal to 0.025 m from a depth of 0.75–1.5 m, and equal to 0.05 m elsewhere in the simulation domain. No flow boundary conditions for both water and PCE were enforced at the top and bottom of the model domain, and hydrostatic pressure boundary conditions were employed at the left and right boundaries (referenced to atmospheric pressure at the domain surface). The cumulative mass balance error (Abriola et al., 1992) was less than 2×10^{-11}% for the PCE entrapment simulations presented herein.

In the absence of interphase mass transfer and reactions, the final long-term NAPL saturation distribution in homogeneous sands is controlled primarily by the values of S_{ro}, S_{ot}, and S_{oi}. Fig. 1 shows the PCE saturation distribution with depth after 360 days for a one-dimensional F35-F50 system having organic-wet mass fractions of 0, 0.25, 0.50, 0.75, and 1.00. Observe that higher NAPL saturation values and a lower infiltration depth occur for the water-wet soil due to the higher S_{ot} value in this soil. In contrast, for the other soils (0.25, 0.50,0.75, and 1.00), the final NAPL distribution is controlled primarily by the value of S_{oi}. Recall that S_{oi} increases with increasing F_o and S_{omax}. The value of S_{omax} in turn is inversely related to the organic relative permeability. Since the organic relative permeability at a given saturation decreases with increasing organic-wet mass fraction, the

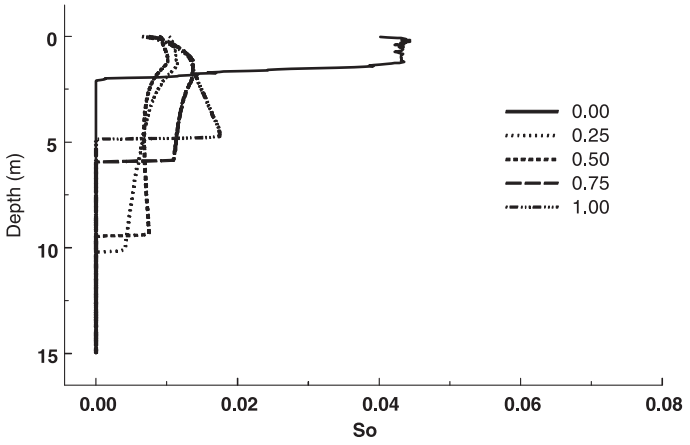

Fig. 1. The PCE saturation distribution with depth after 360 days for F35-F50 porous media having organic-wet mass fractions of 0.0, 0.25, 0.50, 0.75, and 1.00.

value of S_{oi} also increases with increasing F_o. A trend of increasing NAPL saturation and decreasing infiltration depth is therefore observed in Fig. 1 with increasing organic-wet mass fraction.

Analogous simulations to those shown in Fig. 1 were conducted to explore the influence of S_{ro} on the final NAPL saturation distribution. When the value of S_{ro} is set equal to 0.1, the trends observed in Fig. 1 were preserved. Changes in S_{ro} primarily affect the magnitude and shape of the saturation distributions. Increasing S_{ro} tended to increase the maximum retained NAPL saturation and therefore decreased the infiltration depth.

Fig. 2 shows the PCE saturation distribution with depth after 360 days for F70-F110 porous media having organic-wet mass fractions equal to 0.0, 0.25, 0.50, and 1.00. Here

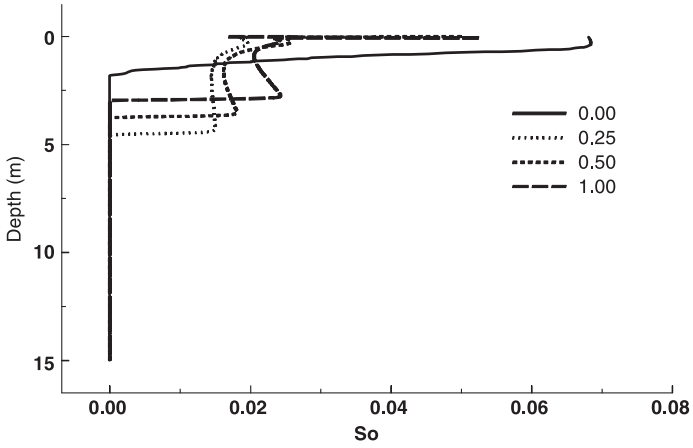

Fig. 2. The PCE saturation distribution with depth after 360 days for F70-F110 porous media having organic-wet mass fractions equal to 0.0, 0. 25, 0.50, and 1.00.

again experimental values of S_{ro} given in Table 1 were used in the simulations. Comparison of Figs. 1 and 2 reveals similar trends in the maximum NAPL saturation and infiltration depth with increasing organic-wet mass fractions. Higher NAPL saturations and lower infiltration depths occur in the finer textured F70-F110 media (Fig. 2) compared to F35-F50 sand (Fig. 1) as a result of decreases in intrinsic permeability and an associated increase in S_{omax}; i.e., S_{oi} increases with decreasing intrinsic permeability. Comparison of Figs. 1 and 2 also reveals that PCE infiltration depth is more sensitive to organic-wet fraction as intrinsic permeability increases.

To explore the influence of spatial variations in subsurface wettability characteristics on PCE entrapment, two-dimensional PCE infiltration and redistribution simulations were conducted for water-wet F35-F50 porous media with various mass fractions of organic-wet sand lenses (1 m high by 2.5 m wide) embedded in the center of the model domain. Fig. 3a–e shows the spatial distribution of PCE after 360 days when the F35-F50 sand lens has organic-wet mass fractions equal to 0.0, 0.25, 0.50, 0.75, and 1.00, respectively. The black box in the figure denotes the boundary of the sand lens. Note in Fig. 3a that the system is homogeneous when the organic-wet fraction of the lens equals zero. Comparison of the simulation results reveals that the distribution of PCE in the sand lens is highly dependent on the wettability of the lens. In Fig. 3c–e, PCE does not displace water from the underlying water-wet soil due to the formation of a capillary barrier at this interface; i.e., the PCE entry pressure of the underlying soil was not exceeded. In contrast, observe in Fig. 3b ($F_o = 0.25$) that the strength of the capillary barrier is not great enough to completely halt the migration of PCE into the underlying water-wet F35-F50 soil. Collectively, simulation results in Fig. 3 demonstrate that contrasts in subsurface wettability characteristics can create regions of high organic liquid saturation in physically homogeneous subsurface systems.

Similar to Fig. 3, Fig. 4 presents a plot of the spatial distribution of PCE after 360 days when various sand lenses (1 m high by 2.5 m wide) were embedded in the center of water-wet F35-F50 sand. In Fig. 4a,b, however, the lenses are water-wet F20-F30 and F70-F110 sands, respectively. Observe that the PCE is at residual saturation directly below the injection point. PCE pooling and spreading occurs at the top of the F70-F110 lens (Fig. 4b) and at the bottom of the F20-F30 lens (Fig. 4a). A capillary barrier occurs at these locations due to physical heterogeneity (pore size), and the migration of PCE from coarser to finer sand is therefore inhibited (In Fig. 4a, from F20-F30 to F35-F50; in Fig. 4b, from F35-F50 to F70-F110). The strength of the capillary barrier increases with increasing capillary contrast; i.e., the difference in PCE entry pressures (cf. Table 1) for F20-F30 to F35-F50 sands, and for F35-F50 to F70-F110, sands is 10.12 and 27.27 cm of water pressure, respectively. In Fig. 4b, the strength of the capillary barrier was sufficient to allow some of the free product NAPL to cascade around the sides of the F70-F110 lens and become entrapped as residual NAPL. In contrast, the strength of the capillary barrier was weaker in Fig. 4a, and PCE penetrated the F35-F50 sand and migrated below the (F20-F30 to F35-F50) interface.

In Fig. 4c,d, the lenses consist of organic-wet F20-F30 and F70-F110 sand, respectively. The PCE is again at residual saturation directly below the injection point. In contrast to Fig. 4b, observe in Fig. 4d that the organic-wet F70-F110 sand lens does not act as a capillary barrier to infiltrating PCE. In Fig. 4c,d capillary forces in the organic-wet

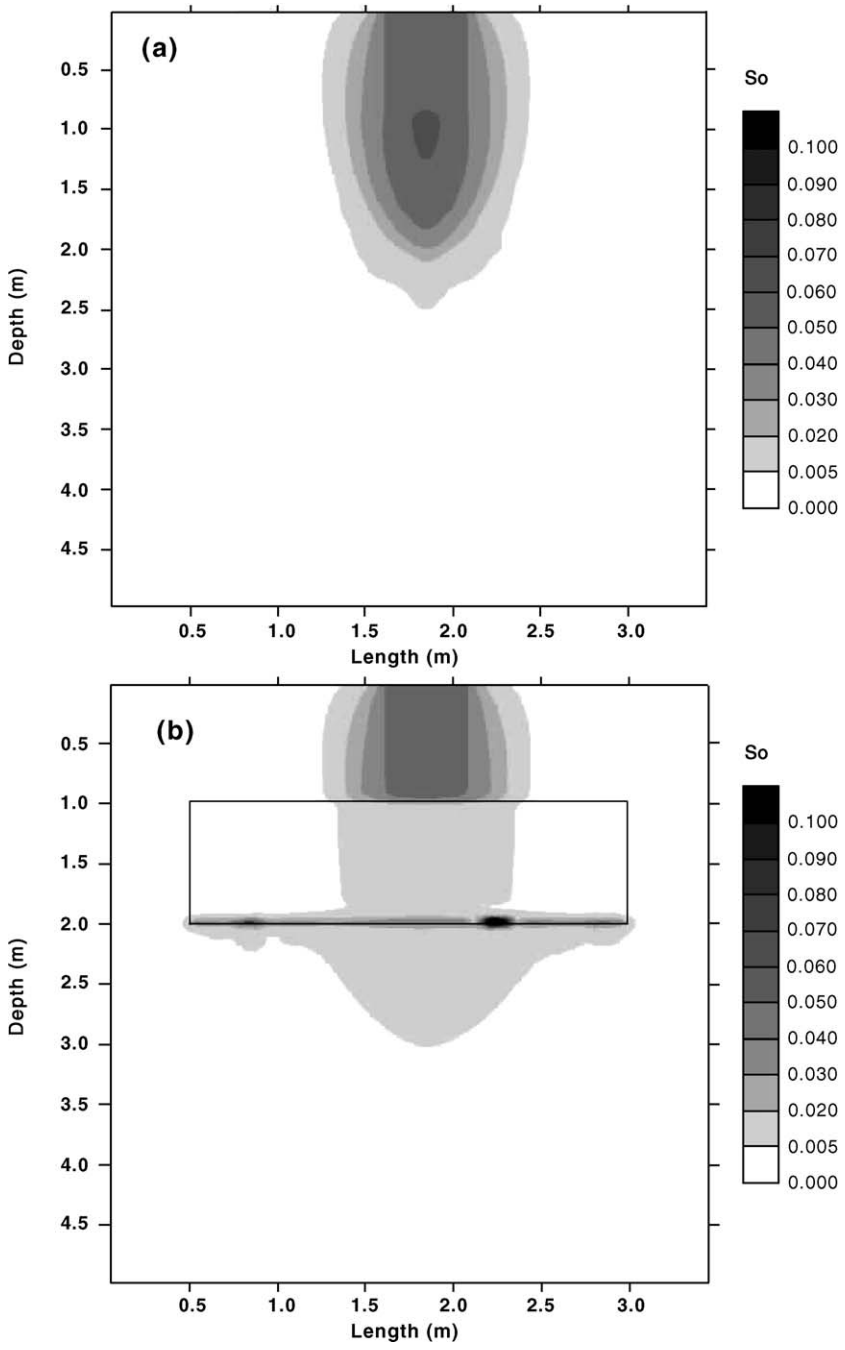

Fig. 3. The spatial distribution of PCE after 360 days when variously wetted F35-F50 sand lenses (1 m high by 2.5 m wide—boundary denoted by the black box) are embedded in the center of water-wet F35-F50 sand. In (a–e), the organic-wet mass fraction of the sand lens equals 0.0, 0.25, 0.50, 0.75, and 1.00, respectively.

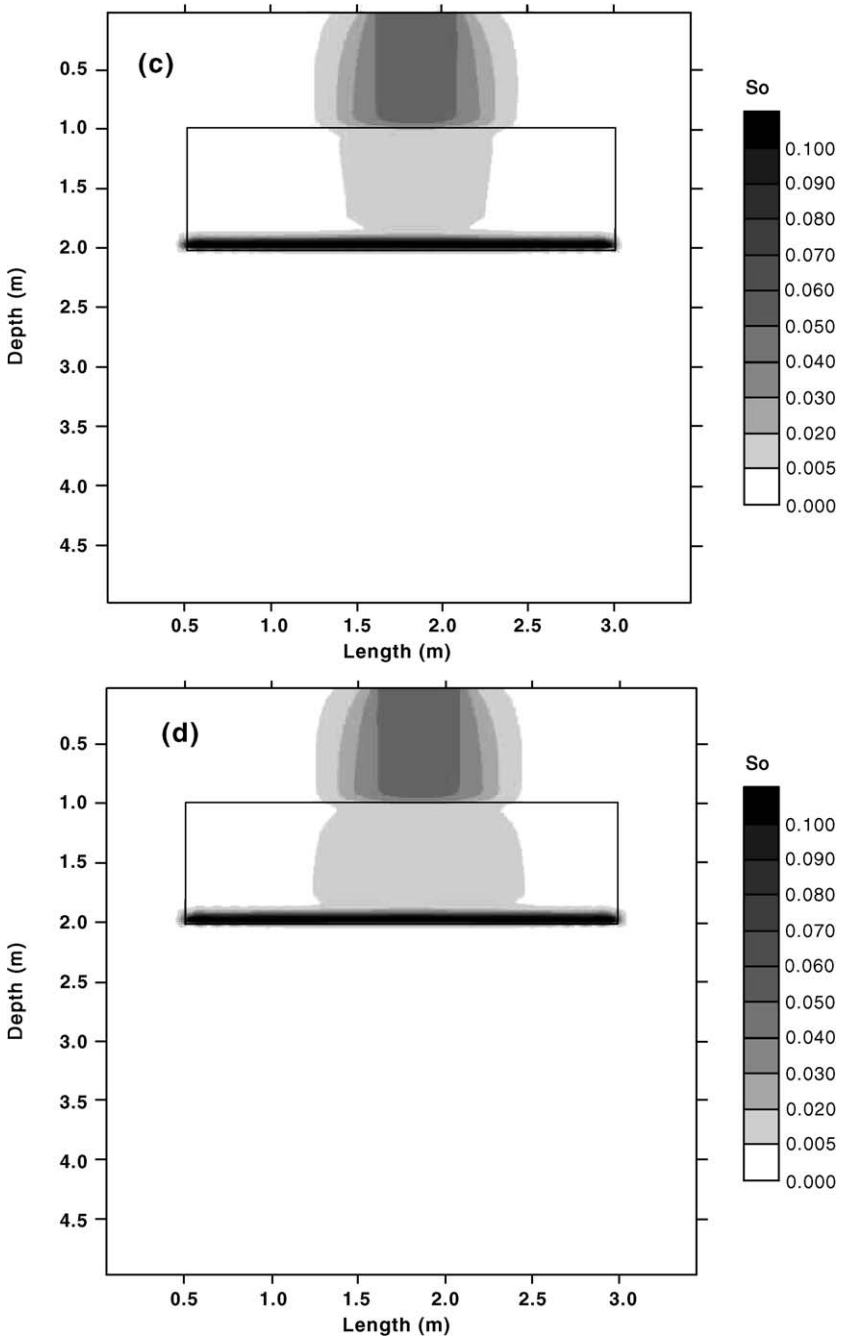

Fig. 3 (*continued*).

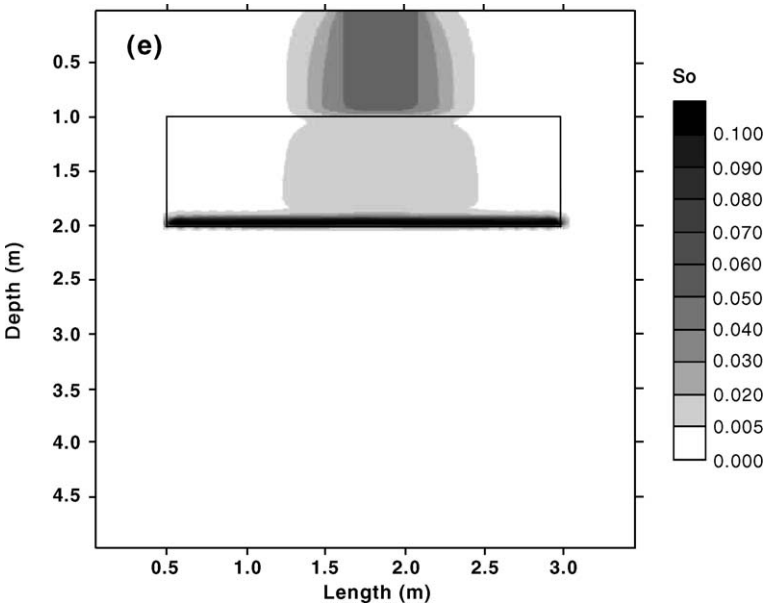

Fig. 3 (*continued*).

lenses actually enhance the infiltration of PCE into these lenses. These same forces create a very effective capillary barrier, high PCE saturations, and enhanced lateral spreading at the lower boundary of the lens. Comparison of Fig. 4c,d reveals that higher PCE saturations occur at the lower lens boundary for the coarser (Fig. 4c, F20-F30) than for the finer (Fig. 4d, F70-F110) organic-wet sand lens. This observation is somewhat counter intuitive, since the magnitude of capillary contrast between F30-F50 sand is greater for F70-F110 than for F20-F30 organic-wet sand. Inspection of Fig. 4d, however, reveals that the lower permeability and increased magnitude of capillary forces in the F70-F110 lens (in comparison to Fig. 4c) results in higher PCE saturations throughout the lens and therefore a lower PCE saturation at the bottom.

In summary, Figs. 3 and 4 demonstrate that the coupled influence of heterogeneity in soil texture, and wettability controls the formation of subsurface capillary barriers. Capillary barrier performance can be enhanced or diminished by the presence of subsurface wettability variations. For example, Fig. 4a,c indicate that increasing the organic-wet fraction of a coarser-textured lens results in an increase in strength of the capillary barrier at the bottom of the lens. In contrast, Fig. 4b,d demonstrate that increasing the organic-wet fraction of a finer-textured lens results in a decrease in strength of the capillary barrier at its top surface.

3.2. Dissolution

This section discusses the simulated dissolution behavior of residual NAPL in the source zone. Before initiating dissolution simulations, two-dimensional simulations of

PCE infiltration and redistribution were conducted using MVALOR (cf. Figs. 3 and 4). For natural groundwater flow conditions (no pumping), PCE migration typically occurs over a much shorter time scale than PCE dissolution. For simplicity and convenience, the simulated PCE flow and transport processes have decoupled herein. The model domain, nodal spacing, and boundary conditions for MVALOR simulations were discussed in Section 3.1. The final organic saturation distribution from MVALOR served as the initial conditions for the MISER dissolution simulations. A corresponding domain size and nodal spacing was utilized for MISER simulations. No flow boundary conditions were enforced at the top and bottom of the MISER model domain, while a 2% hydraulic gradient was maintained throughout the domain using constant pressure boundary conditions on the left and right hand sides (flow from left to right). Model simulations were continued until all the NAPL was completely dissolved (less than 0.003% of the initial NAPL mass remaining) from the simulation domain.

The MISER code uses nodal specific fluxes, thereby eliminating discontinuities in the velocity field that are present when using element average velocities. The use of a continuous velocity field has been shown to yield significant improvements in mass balance for the transport equation (Yeh, 1981). Temporal error is controlled via limits on the number of iterations the solver takes per time step. The cumulative mass balance error (Abriola et al., 1997) for PCE during the dissolution simulations was less than 1.74×10^{-1}%.

In addition to the previously presented fluid/matrix properties (density, viscosity, interfacial tension, and hydraulic property model parameters), relevant PCE transport properties that were used in the simulations include an equilibrium solubility of approximately 203 mg l^{-1} at 20 °C (Bradford et al., 1999), and an aqueous phase diffusion coefficient of 6.56×10^{-6} cm^2 s^{-1} (Hayduk and Laudie, 1974). The horizontal and vertical dispersivities were selected to be 0.35 and 0.035 m, respectively.

Two-dimensional PCE entrapment and dissolution simulations were conducted for uniform F35-F50 porous media having organic-wet mass fractions equal to 0.0, 0.25, 0.50, 0.75, and 1.00. To minimize NAPL pooling at the bottom boundary (only the $F_o = 0.25$ had slight pooling at the bottom boundary), PCE injection was continued for only 0.75 days (half the PCE volume of other simulations). Fig. 5 presents a plot of the average effluent concentration as a function of water volume exiting along the right boundary. Since the intrinsic permeability of the F35-F50 sand is independent of wettability, the volume of water given in the figure can be related to a dissolution time by dividing by the approximate water flux of 4700 l day^{-1}. The dissolution time is shortest for the $F_o = 0.50$ and longest for the $F_o = 0.0$ system. Intermediate PCE dissolution times occurred in the other soil wettability systems. Bradford et al. (1999) presented soil column dissolution data for residual PCE entrapped in fractional wettability F35-F50 sand. For similar NAPL saturations, these authors observed a trend of decreasing remediation time with increasing organic-wet mass fraction of the soil. A similar trend is observed in Fig. 5 for PCE dissolution in soils having F_o equal to 0.0, 0.25, and 0.50. In contrast, PCE dissolution in soils having F_o equal to 0.75 or 1.00 actually exhibits a slightly longer dissolution time than the $F_o = 0.50$ system. An explanation is obtained by considering the spatial distribution of NAPL in these systems. Similar to Fig. 1, two-dimensional entrapment simulations reveals that the source zone area (region with $S_o > 0.001$) increases in the

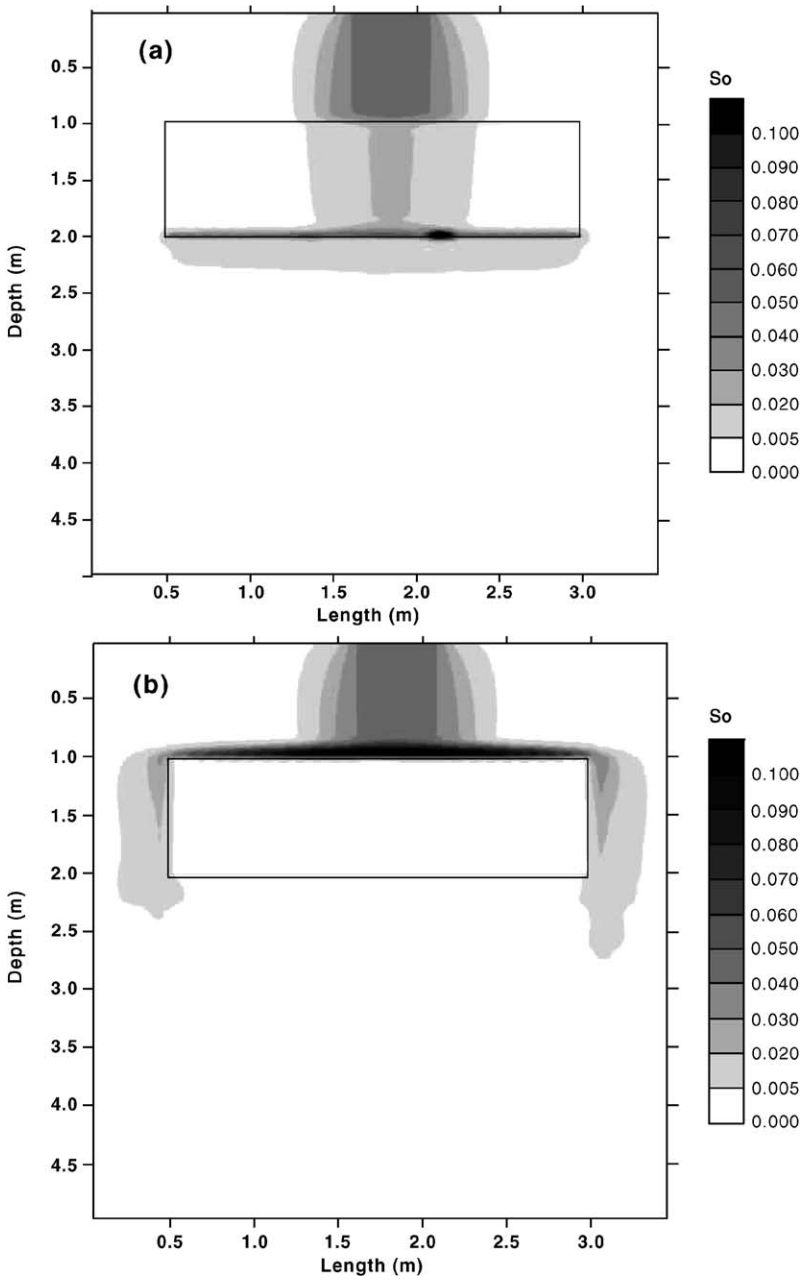

Fig. 4. A plot of the spatial distribution of PCE after 360 days when various sand lenses (1 m high by 2.5 m wide—boundary denoted by the black box) were embedded in the center of water-wet F35-F50 sand. In (a) and (b), the lens consists of water-wet F20-F30 and F70-F110 sand, respectively, whereas in (c) and (d), the lens consists of organic-wet F20-F30 and F70-F110 sand, respectively.

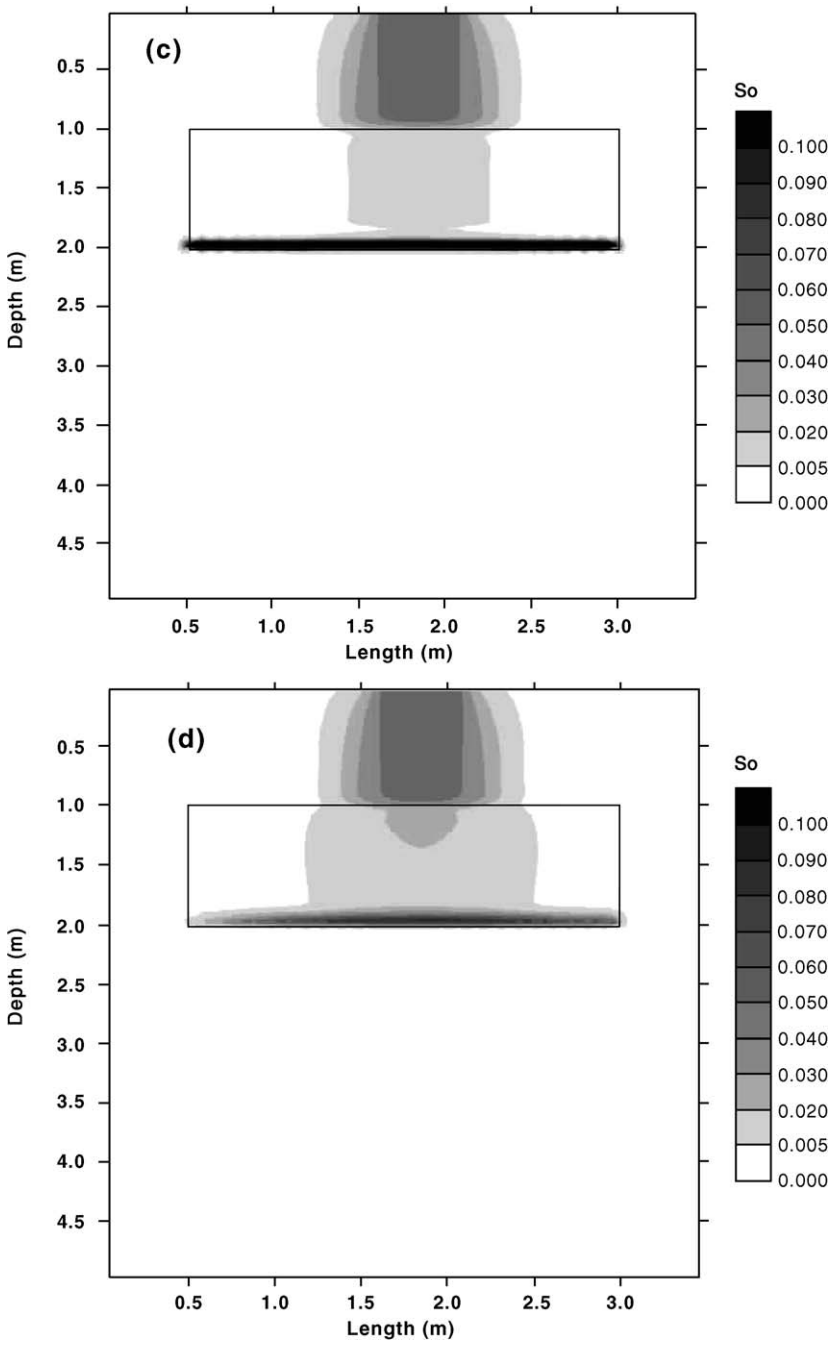

Fig. 4 (*continued*).

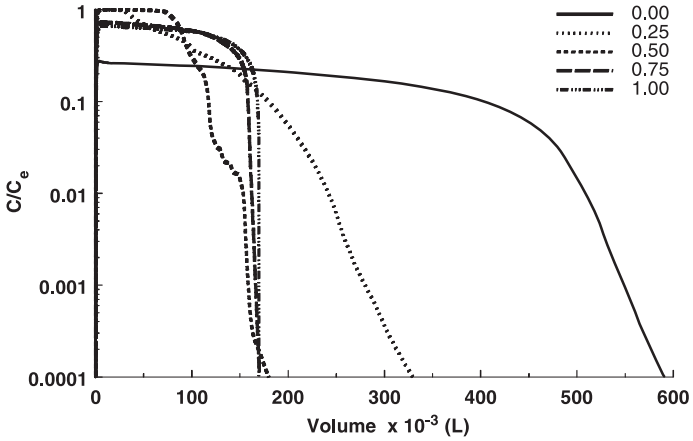

Fig. 5. Simulated dissolution behavior for PCE retained in F35-F50 porous media having organic-wet mass fractions equal to 0.0, 0.25, 0.50, 0.75, and 1.00. The figure presents a semilog plot of the average normalized effluent concentration (C/C_e) as a function of water volume exiting along the right boundary.

following order: $F_o = 0.25 > 0.50 > 0.75 > 1.00 > 0.0$. Dissolution is facilitated in systems with a higher source zone area due to lower NAPL saturations and a corresponding higher water permeability. Hence, Fig. 5 suggests that the mass transfer rate (increases with increasing organic-wet fraction) and distribution are important factors in determining the remediation time of NAPL contaminants.

To further highlight the influence of NAPL distribution on dissolution time, additional entrapment and dissolution simulations were conducted for water-wet F35-F50 porous media having various organic-wet mass fractions (0, 0.25, 0.50, 0.75, 1.00) sand lenses (1 m high by 2.5 m wide) embedded in the center of the model domain. The PCE entrapment behavior was presented earlier in Fig. 3. The system is homogeneous for the $F_o = 0$ sand lens. Fig. 6 presents a plot of the average effluent concentration as a function of water volume exiting along the right boundary. The shape of the effluent concentration curve is dependent on the wettability of the sand lens. For relative effluent concentrations greater than 0.0001, the $F_o = 0.50$ sand lens system has the slowest dissolution time, whereas the $F_o = 0.75$ and 1.00 sand lens systems exhibit slightly faster dissolution times. In these systems, the spatial distribution of PCE (cf. Fig. 3c,d,e) is quite similar, and differences in the effluent concentration curves are therefore attributed to the increased dissolution rate (Bradford et al., 1999) and water relative permeability (Bradford et al., 1997) with increasing organic-wet sand fractions.

In contrast, Fig. 6 indicates that the homogeneous $F_o = 0$ system exhibits a more rapid dissolution behavior than the heterogeneous $F_o = 0.5$, 0.75, and 1.00 lens systems. Since the $F_o = 0$ system has a lower dissolution rate than the $F_o = 0.5$, 0.75, and 1.00 sands (Bradford et al., 1999), differences in the effluent concentration curves can be ascribed primarily to the spatial distribution of PCE. The presence of capillary barriers in the heterogeneous $F_o = 0.5$, 0.75, and 1.00 lens systems produce higher PCE saturations and an associated decrease in water permeability than the homogeneous $F_o = 0$ system (cf. Fig. 3). The $F_o = 0.25$ sand lens system has the highest effluent concentrations initially, achieves

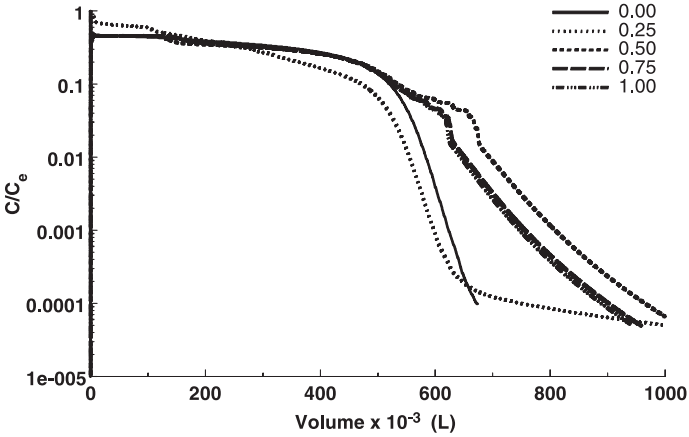

Fig. 6. Simulated dissolution behavior for PCE retained in water-wet F35-F50 sand containing variously wetted F35-F50 sand lenses (cf. Fig. 3a–e). The figure presents a semilog plot of the average normalized effluent concentration (C/C_e) as a function of water volume exiting along the right boundary.

relative effluent concentrations lower than 0.00011 the most rapidly, and then exhibits persistent concentration tailing at low concentration levels. The initial rapid dissolution behavior for PCE in the $F_o = 0.25$ sand lens system is due to the lower PCE saturations that are distributed over a larger region (cf. Fig. 3b), and the enhanced dissolution rate compared to the uniform water-wet soil. The low concentration tailing behavior occurs due to the presence of a weak capillary barrier that produces high PCE saturations that dissolve at a slower rate compared than the $F_o = 0.5$, 0.75, and 1.00 lens systems. Comparison of Figs. 5 and 6 reveals that NAPL distribution is very important in determining dissolution times. For example, the dissolution time for PCE in the $F_o = 0.50$ system is shortest in Fig. 5 and longest in Fig. 6.

Two-dimensional PCE entrapment and dissolution simulations were conducted for water-wet F35-F50 porous media having various water-wet sand (F20-F30, F35-F50, and F70-F110) lenses (1 m high by 2.5 m wide) embedded in the center of the model domain. The F35-F50 sand lens system is physically homogeneous. The PCE entrapment behavior was discussed earlier in Figs. 3 and 4. Fig. 7 presents a plot of the average effluent concentration as a function of water volume exiting along the right boundary for these water-wet systems. Observe that the volume of water required to dissolve the PCE increases in the following order: uniform F35-F50 < F70-F110 lens system ≪ F20-F30 lens system. Due to the presence of a capillary barrier in the F70-F110 system, Fig. 4b indicates that PCE is retained exclusively in the F35-F50 sand adjacent to the F70-F110 lens. Differences in the dissolution behavior of the uniform F35-F50 system and F70-F110 lens system are therefore primarily due to differences in the spatial distribution of PCE. The presence of a capillary barrier in the F70-F110 lens system leads to high PCE saturations (Fig. 4b) that are associated with a reduction in water relative permeability in the source zone. Furthermore, the lower intrinsic permeability of the F70-F110 lens shields the PCE on the downstream side of the lens from flowing water. All of these factors account for the greater volume of water required to dissolve the PCE in the F70-F110 system compared to

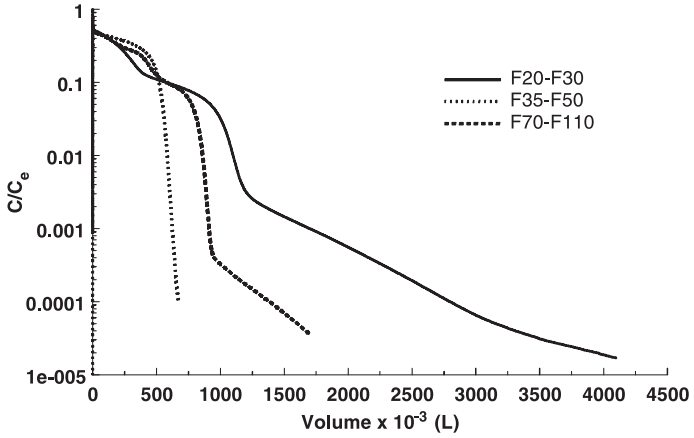

Fig. 7. Simulated dissolution behavior for PCE retained in water-wet F35-F50 sand containing water-wet sand lenses of various soil textures (cf. Figs. 3a and 4a,b). The figure presents a semilog plot of the average normalized effluent concentration (C/C_e) as a function of water volume exiting along the right boundary.

the uniform F35-F50 system. The F20-F30 lens system requires the largest volume of water to dissolve PCE in the source zone because of flow bypassing of the PCE retained at the bottom boundary of the F20-F30 lens. A much greater volume of water flows through the F20-F30 system due to differences in the intrinsic permeability of the lens sand. The approximate water flux flowing out of the water-wet F20-F30, F35-F50, and F70-F110 systems is 9700, 4700, and 3800 l day^{-1}, respectively.

To explore the coupled influence of heterogeneity in soil texture and wettability, two-dimensional PCE entrapment and dissolution simulations were conducted for water-wet F35-F50 porous media having various organic-wet sand (F20-F30, F35-F50, and F70-F110) lenses (1 m high by 2.5 m wide) embedded in the center of the model domain. The PCE entrapment behavior was discussed earlier in Figs. 3 and 4. Fig. 8 presents a plot of the average effluent concentration as a function of water volume exiting along the right boundary for these systems. Observe that the volume of water required to dissolve PCE in the source zone increases in the following order: F35-F50 < F70-F110 ≪ F20-F30 organic-wet lens systems. Since similar PCE dissolution rates were observed in organic-wet F20-F30, F35-F50, and F70-F110 sand (Bradford et al., 2000), an explanation of the behavior shown in Fig. 8 is obtained by considering the aqueous phase flow field and the spatial PCE saturation distribution. Figs. 3e and 4c,d indicate that each of the organic-wet lens (F20-F30, F35-F50, and F70-F110) acted as an effective capillary barrier, retaining the PCE in the lens. The spatial distribution within the lens, however, is not the same. The F70-F110 lens system has higher PCE saturations distributed throughout the lens than the other systems. Due to differences in the lens intrinsic permeability, much more water flows through the F20-F30 (9700 l day^{-1}) than the F35-F50 (4700 l day^{-1}) or F70-F110 (3800 l day^{-1}) organic-wet lens systems. As for the water-wet lens systems (Fig. 7), the greatest volume of water is required to dissolve PCE in the F20-F30 organic-wet lens system because of flow bypassing of the high PCE saturations spread along the bottom boundary of this lens. The F70-F110 organic-wet lens system exhibits higher effluent concentration

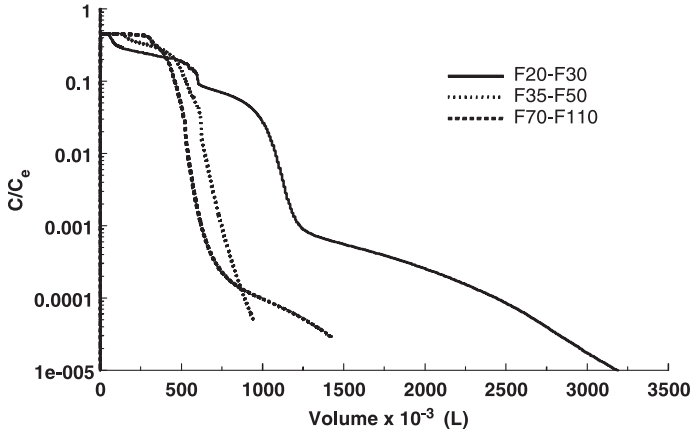

Fig. 8. Simulated dissolution behavior for PCE retained in water-wet F35-F50 sand containing organic-wet sand lenses of various soil textures (cf. Figs. 3e and 4c,d). The figure presents a semilog plot of the average normalized effluent concentration (C/C_e) as a function of water volume exiting along the right boundary.

initially and earlier reduction in effluent concentrations due to the more dispersed distribution of PCE throughout the source zone (cf. Fig. 4). The concentration tailing behavior of the F70-F110 organic-wet lens system is due to flow bypassing of the high PCE saturations at the bottom boundary of the lens, which is facilitated by the lower intrinsic permeability of the F70-F110 sand. Variations in the aqueous phase flow field are not as pronounced in the F35-F50 organic-wet lens system, and the effluent concentration curve therefore decreases more uniformly than in the other organic-wet lens systems.

4. Summary and conclusions

Refined conceptual models for NAPL entrapment and dissolution were implemented in existing two-dimensional NAPL flow and transport simulators. Independently determined hydraulic properties, residual saturations, and dissolution parameters for soils encompassing a range in grain-size and wettability characteristics were then used in conjunction with the numerical simulators to explore the influence of heterogeneity in soil texture and wettability on NAPL entrapment and dissolution.

NAPL infiltration and redistribution simulations demonstrate that the spatial distribution of residual NAPL (after 360 days) is highly dependent on the subsurface wettability characteristics. In physically homogeneous systems the final saturation distribution depends on the values of the residual, entrapped, and immobile (coating NAPL-wet solid surfaces) NAPL saturations. For a given soil, the NAPL infiltration depth was found to be maximum at intermediate organic-wet mass fractions ($F_o = 0.25$). This observation was attributed to the fact that NAPL entrapment is inhibited by the presence of NAPL-wet solid surfaces and by associated decreases in the immobile NAPL saturation. Conversely, NAPL infiltration depth was minimum for strongly wetted soils (water-wet or organic-wet). This occurs because NAPL entrapment is maximum in water-wet soils, and the

immobile NAPL saturation is maximum in organic-wet soils. The soil intrinsic and relative permeability also influence the spatial distribution of NAPL by affecting the historic maximum NAPL saturation. Decreasing the NAPL conductivity leads to higher NAPL saturations and, consequently, enhances NAPL retention.

In heterogeneous systems the final distribution of NAPL is also controlled by the presence of subsurface capillary barriers. Capillary barriers occur as a result of abrupt changes in capillary characteristics (pore-size distribution or wettability characteristics) which retain or exclude the NAPL at this interface. NAPL pooling and spreading occurs at the interface of capillary contrast due to an inhibition of the downward migration of NAPL. Numerical simulations demonstrate that the performance of soil texture-induced capillary barriers can be enhanced or diminished by the presence of subsurface wettability variations.

Numerical simulations were also conducted to explore the dissolution behavior of residual NAPL in heterogeneous porous media. In physically homogeneous systems, the dissolution behavior was found to be strongly dependent on the soil wettability, as well as the spatial NAPL distribution. For similar dissolution rates, NAPL distributions that are distributed over a larger region are remediated more rapidly because the aqueous phase relative permeability is greater. In heterogeneous systems, the dissolution behavior was found to be highly dependent on the spatial NAPL distribution. Spatial distributions of soil texture and wettability that produced strong capillary barriers and higher NAPL saturations tended to exhibit longer dissolution times than comparable homogeneous systems. Numerical simulations suggest a complex interaction between the remediation time and the NAPL saturation distribution, aqueous phase flow field, and mass transfer characteristics. The relative importance of each of these factors depends on the degree and type of heterogeneity.

Acknowledgements

Funding for this research was in part provided by the National Institute of Environmental Health Sciences (NIEHS) under Grant # ES04911 and by the Department of Energy (DOE) under Grant # DE-FG07-96ER14702. The research described in this article has not been subject to NIEHS or DOE review and, therefore, does not necessarily reflect the views of these organizations, and no official endorsement should be inferred.

References

Abriola, L.M., 1989. Modeling multiphase migration of organic chemicals in groundwater systems—a review and assessment. Environ. Health Perspect. 83, 117–143.

Abriola, L.M., Rathfelder, K.M., 1993. Mass balance errors in modeling 2-phase immiscible flows—causes and remedies. Adv. Water Resour. 16, 223–239.

Abriola, L.M., Rathfelder, K., Maiza, M., Yadav, S., 1992. VALOR code version 1.0: a PC code for simulating immiscible contaminant transport in subsurface systems. EPRI TR-101018, Project 2879-08. Final Report.

Abriola, L.M., Lang, J., Rathfelder, K., 1997. Documentation for: Michigan Soil-Vapor Extraction Remediation

(MISER) Model—A Computer Program to Model Soil Vapor Extraction and Bioventing of Organic Chemicals in Unsaturated Geological Material. EPA/600/R-97/099. United States Environmental Protection Agency, Washington, DC.

Anderson, W.G., 1986. Wettability literature survey: Part 1. Rock/oil/brine interactions and the effects of core handling on wettability. J. Pet. Technol. 38, 1125–1144.

Anderson, M.R., Johnson, R.L., Pankow, J.F., 1992. Dissolution of dense chlorinated solvents into ground water: 1. Dissolution from a well-defined residual source. Ground Water 30, 250–256.

Berglund, S., 1997. Aquifer remediation by pumping: a model for stochastic–advective transport with nonaqueous phase liquid dissolution. Water Resour. Res. 33, 649–661.

Bradford, S.A., Abriola, L.M., 2001. Dissolution of residual tetrachloroethylene in fractional wettability porous media: incorporation of interfacial area estimates. Water Resour. Res. 37, 1183–1195.

Bradford, S.A., Leij, F.J., 1995a. Fractional wettability effects on two- and three-fluid capillary pressure–saturation relations. J. Contam. Hydrol. 20, 89–109.

Bradford, S.A., Leij, F.J., 1995b. Wettability effects on scaling two- and three-fluid capillary pressure–saturation relations. Environ. Sci. Technol. 29, 1446–1455.

Bradford, S.A., Leij, F.J., 1996. Predicting two- and three-fluid capillary pressure–saturation relations in mixed wettability media. Water Resour. Res. 32, 251–259.

Bradford, S.A., Leij, F.J., 1997. Estimating interfacial areas for multi-fluid soil systems. J. Contam. Hydrol. 27, 83–105.

Bradford, S.A., Abriola, L.M., Leij, F.J., 1997. Wettability effects on two- and three-fluid relative permeabilities. J. Contam. Hydrol. 28, 171–191.

Bradford, S.A., Abriola, L.M., Rathfelder, K.M., 1998. Flow and entrapment of dense nonaqueous phase liquids in physically and chemically heterogeneous aquifer formations. Adv. Water Resour. 22, 117–132.

Bradford, S.A., Vendlinski, R.A., Abriola, L.M., 1999. The entrapment and long-term dissolution of tetrachloroethylene in fractional wettability porous media. Water Resour. Res. 35, 2955–2964.

Bradford, S.A., Phelan, T.J., Abriola, L.M., 2000. Dissolution of residual tetrachloroethylene in fractional wettability porous media: correlation development and application. J. Contam. Hydrol. 45, 35–61.

Chatzis, I., Morrow, N.R., Lim, H.T., 1983. Magnitude and detailed structure of residual oil saturation. Soc. Pet. Eng. J. 23, 311–326.

Dekker, T.J., Abriola, L.M., 2000. The influence of field-scale heterogeneity on the infiltration and entrapment of dense nonaqueous phase liquids in saturated formations. J. Contam. Hydrol. 42, 187–218.

Dekker, L.W., Ritsema, C.J., 1994. How water moves in a water repellent sandy soil: 1. Potential and actual water repellency. Water Resour. Res. 30, 2507–2519.

Demond, A.H., Roberts, P.V., 1991. Effect of interfacial forces on two-phase capillary pressure–saturation relationships. Water Resour. Res. 27, 423–437.

Demond, A.H., Desai, F.N., Hayes, K.F., 1994. Effect of cationic surfactants on organic liquid–water capillary pressure–saturation relationships. Water Resour. Res. 30, 333–342.

Demond, A.H., Rathfelder, K.M., Abriola, L.M., 1996. Simulation of organic liquid flow in porous media using estimated and measured transport properties. J. Contam. Hydrol. 22, 223–239.

Essaid, H.I., Herkelrath, W.N., Hess, K.M., 1993. Simulation of fluid distributions observed at a crude oil spill site incorporating hysteresis, oil entrapment, and spatial variability of hydraulic properties. Water Resour. Res. 29, 1753–1770.

Geller, J.T., Hunt, J.R., 1993. Mass transfer from nonaqueous phase organic liquids in water-saturated porous media. Water Resour. Res. 29, 833–846.

Guarnaccia, J.F., Imhoff, P.T., Missildine, B.C., Oostrom, M., Celia, M.A., Dane, J.H., Jaffe, P.R., Pinder, G.F., 1992. Multiphase Chemical Transport in Porous Media, Final Report, EPA/600/S-92/002. U.S. Environ. Protect. Agency, Washington, DC.

Hayduk, W., Laudie, H., 1974. Prediction of diffusion coefficients for nonelectrolytes in dilute aqueous solutions. AIChE J. 20, 611–615.

Hunt, J.R., Sitar, N., Udell, K.S., 1988. Nonaqueous phase liquid transport and cleanup: 1. Analysis of mechanisms. Water Resour. Res. 24, 1247–1258.

Imhoff, P.T., Jaffe, P.R., Pinder, G.F., 1994. An experimental study of complete dissolution of a nonaqueous phase liquid in a saturated porous media. Water Resour. Res. 30, 307–320.

Imhoff, P.T., Frizzell, A., Miller, C.T., 1997. Evaluation of thermal effects on the dissolution of a nonaqueous phase liquid in porous media. Environ. Sci. Technol. 31, 1615–1622.

Klute, A., Dirksen, C., 1986. Hydraulic conductivity and diffusivity: laboratory methods. In: Klute, A. (Ed.), Method of Soil Analysis, Part 1. Physical and Mineralogical Methods, 2nd ed. Soil Science Society of America, Madison, WI, pp. 687–734.

Kueper, B.H., Frind, E.O., 1991. Two-phase flow in heterogeneous porous media: 2. Model application. Water Resour. Res. 27, 1059–1070.

Kueper, B.H., Abbott, W., Farquhar, G., 1989. Experimental observations of multiphase flow in heterogeneous porous media. J. Contam. Hydrol. 5, 83–95.

Kueper, B.H., Redman, D., Starr, R.C., Reitsma, S., Mah, M., 1993. A field experiment to study the behavior of tetrachloroethylene below the water table: spatial distribution of residual and pooled DNAPL. Ground Water 31, 756–766.

Land, C.S., 1968. Calculation of imbibition relative permeability for two- and three-phase flow from rock properties. Soc. Pet. Eng. J. 8, 149–156.

Leverett, M.C., 1941. Capillary behavior in porous solids. Trans. Am. Inst. Min. Metall. Pet. Eng. 142, 152–169.

Mayer, A.S., Miller, C.T., 1996. The influence of mass transfer characteristics and porous media heterogeneity on nonaqueous phase dissolution. Water Resour. Res. 32, 1551–1567.

Miller, C.T., Poirier-McNeill, M.M., Mayer, A.S., 1990. Dissolution of trapped nonaqueous phase liquids: mass transfer characteristics. Water Resour. Res. 26, 2783–2796.

Miller, C.T., Christakos, G., Imhoff, P.T., McBride, J.F., Pedit, J.A., Trangenstein, J.A., 1998. Multiphase flow and transport modeling in heterogeneous porous media: challenges and approaches. Adv. Water Resour. 21, 77–120.

Morrow, N.R., 1970. In: de Wiest, R.J.M. (Ed.), Physics and thermodynamics of capillary action in porous media. Flow through porous media. Academic Press, New York, pp. 104–128.

National Research Council, 1994. Alternatives for Ground Water Cleanup. National Academy Press, Washington, DC.

O'Carroll, D.M., Bradford, S.A., Abriola, L.M., 2001. Infiltration and redistribution of PCE in a system containing spatial wettability variations. J. Contam. Hydrol. (submitted for publication).

Parker, J.C., Lenhard, R.J., 1987. A model for hysteretic constitutive relations governing multiphase flow: 1. Saturation–pressure relations. Water Resour. Res. 23, 2187–2196.

Parker, J.C., Katyal, A.K., Kaluarachchi, J.J., Lenhard, R.J., Johnson, T.J., Jayaraman, K., Jayaraman, K., Unlu, K., Zhu, J.L., 1991. Modeling multiphase organic chemical transport in soils and ground water. Final Report, EPA/600/2-91/042. U.S. Environmental Protection Agency, Washington, DC.

Poulsen, M., Kueper, B.H., 1992. A field experiment to study the behavior of tetrachloroethylene in unsaturated porous media. Environ. Sci. Technol. 26, 889–895.

Powers, S.E., Tamblin, M.E., 1995. Wettability of porous media after exposure to synthetic gasolines. J. Contam. Hydrol. 19, 105–125.

Powers, S.E., Loureiro, C.O., Abriola, L.M., Weber Jr., W.J., 1991. Theoretical study of the significance of nonequilibrium dissolution of nonaqueous phase liquids in subsurface systems. Water Resour. Res. 27, 463–477.

Powers, S.E., Abriola, L.M., Weber Jr., W.J., 1992. An experimental investigation of NAPL dissolution in saturated subsurface systems: steady state mass transfer rates. Water Resour. Res. 28, 2691–2705.

Powers, S.E., Abriola, L.M., Weber Jr., W.J., 1994a. An experimental investigation of NAPL dissolution in saturated subsurface systems: transient mass transfer rates. Water Resour. Res. 30, 321–332.

Powers, S.E., Abriola, L.M., Dunkin, J.S., Weber Jr., W.J., 1994b. Phenomenological models for transient NAPL-water mass-transfer processes. J. Contam. Hydrol. 16, 1–33.

Powers, S.E., Nambi, I.M., Curry Jr., G.W., 1998. Non-aqueous phase liquid dissolution in heterogeneous systems: mechanisms and a local equilibrium modeling approach. Water Resour. Res. 34, 3293–3302.

Rathfelder, K.M., Abriola, L.M., 1998. The influence of capillarity in numerical modeling of organic liquid redistribution in two-phase systems. Adv. Water Resour. 21, 159–170.

Rathfelder, K.M., Lang, J.R., Abriola, L.M., 2000. A numerical model (MISER) for the simulation of coupled physical, chemical, and biological processes in soil vapor extraction and bioventing systems. J. Contam. Hydrol. 43, 239–270.

Rathfelder, K.M., Abriola, L.M., Taylor, T.P., Pennell, K.D., 2001. Surfactant enhanced recovery of tetrachloroethylene from a porous medium containing low permeability lenses: 2. Numerical simulation. J. Contam. Hydrol. 48, 351–374.

Rixey, W.G., 1996. The long-term dissolution characteristics of a residually trapped BTX mixture in soil. Hazard. Waste Hazard. Mater. 13, 197–211.

Saba, T., Illangasekare, T.H., 2000. Effect of groundwater flow dimensionality on mass transfer from entrapped nonaqueous phase liquid contaminants. Water Resour. Res. 36, 971–979.

Wilson, J.L., Conrad, S.H., Mason, W.R., Peplinski, W., Hagan, E., 1990. Laboratory investigation of residual liquid organics from spills, leaks and the disposal of hazardous wastes in groundwater. Final Report, EPA/600/6-90/004. U.S. Environmental Protection Agency, Washington, DC.

Yeh, G.-T., 1981. On the computation of Darcian velocity and mass balance in the finite element modeling of groundwater flow. Water Resour. Res. 17, 1529–1534.